NANO LETTERS

Letter

pubs.acs.org/NanoLett

Two-Dimensional Water-Coupled Metallic MoS_2 with Nanochannels for Ultrafast Supercapacitors

Xiumei Geng,[†] Yelong Zhang,[†] Yang Han,[†] Jingxiao Li,[†] Lei Yang,[†] Mourad Benamara,[‡] Liao Chen,[†] and Hongli Zhu*[,†]

[†]Department of Mechanical and Industrial Engineering, Northeastern University, Boston, Massachusetts 02115, United States

[‡]Institute for Nanoscale Materials Science and Engineering, University of Arkansas, Fayetteville, Arkansas 72701, United States

Supporting Information

ABSTRACT: MoS_2 is a promising electrode material for energy storage. However, the intrinsic multilayer pure metallic MoS_2 (M-MoS_2) has not been investigated for use in supercapacitors. Here, an ultrafast rate supercapacitor with extraordinary capacitance using a multilayer M-MoS_2–H_2O system is first investigated. Intrinsic M-MoS_2 with a monolayer of water molecules covering both sides of nanosheets is obtained through a hydrothermal method with water as solvent. The super electrical conductivity of the as-prepared pure M-MoS_2 is beneficial to electron transport for high power supercapacitor. Meanwhile, nanochannels between the layers of M-MoS_2–H_2O with a distance of ∼1.18 nm are favorable for increasing the specific space for ion diffusion and enlarging the surface area for ion adsorption. By virtue of this, M-MoS_2–H_2O reaches a high capacitance of 380 F/g at a scan rate of 5 mV/s and still maintains 105 F/g at scan rate of 10 V/s. Furthermore, the specific capacitance of the symmetric supercapacitor based on M-MoS_2–H_2O electrodes retain a value as high as 249 F/g under 50 mV/s. These findings suggest that multilayered M-MoS_2–H_2O system with ion accessible large nanochannels and efficient charge transport provide an efficient energy storage strategy for ultrafast supercapacitors.

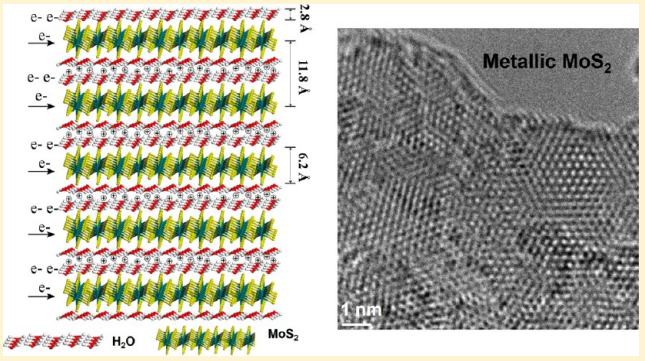

KEYWORDS: *Metallic MoS_2, nanochannels, M-MoS_2–H_2O system, hydrophilic, high electrical conductivity*

Supercapacitor with superior power density and long cycling life has widespread applications in power tools, energy backup system, hybrid electric vehicles, and portable devices. Carbon materials, including active carbon, carbon aerogel, nanocarbon, carbon foam, are the most commonly employed electrode materials due to its good electrical conductivity and high surface area.[1−5] Compared to the excellent carbon-based supercapacitors, supercapacitors that based on two-dimensional transition-metal dichalcogenides such as MoS_2 is lack of exploration. 2H semiconductor phase (S-MoS_2) and 1T metallic phase (M-MoS_2) are two typical crystal structures for MoS_2.[6,7] It is well-known that the low electrical conductivity of 2H semiconductor MoS_2 is a disadvantage for electrochemical energy storage.[6,8] Thus, hybrid electrodes of semiconductor MoS_2 and other high electrical conductivity materials such as graphene and polyanilines are used to improve the electrical conductivity and show moderate electrochemical performance in battery.[9−12] Alternatively, it has been proven that M-MoS_2 has higher electrical conductivity and better hydrophilicity, which is beneficial to obtain higher electron transport efficiency and better ion accessibility, therefore achieving higher electrochemical energy storage performance for the supercapacitor.[13] The sheet resistance is 1.61×10^4 Ω/□ for M-MoS_2 and 2.26×10^9 Ω/□ for S-MoS_2, which correspond to a resistivity of 0.482 Ω·cm for M-MoS2 and 7.68×10^4 Ω·cm for S-MoS_2.[14] The M-MoS_2 has an electrical conductivity that is 5 orders of magnitude higher than that of S-MoS_2. However, the current preparation method for M-MoS_2 based on Li^+ intercalation of S-MoS_2 is complicated, time-consuming, unstable, and dangerous,[15−17] which to some extent would hamper a broad range of applications in clean energy such as supercapacitor and battery. At present, the most lethal defection is that as-prepared MoS_2 is in coexistence with S-MoS_2 and M-MoS_2 with a metallic phase concentration of 50−70%.[18] Though specific volumetric capacitance of ∼700 F/cm^3 has been obtained with metallic phase MoS_2 in aqueous electrolyte, there is no denying that the impurity has a great chance to trigger the phase transformation from metallic phase to semiconducting phase of MoS_2 and degrade the electrochemical storage capacity and reliability.[13] Thus, the electrochemical storage performance for pure metallic phase MoS_2 remains unknown. After we determined the preparation method for pure metallic phase MoS_2 with a hydrothermal method, it was highly desirable to study the

Received: December 12, 2016
Revised: January 22, 2017

© XXXX American Chemical Society

DOI: 10.1021/acs.nanolett.6b05134
Nano Lett. XXXX, XXX, XXX−XXX

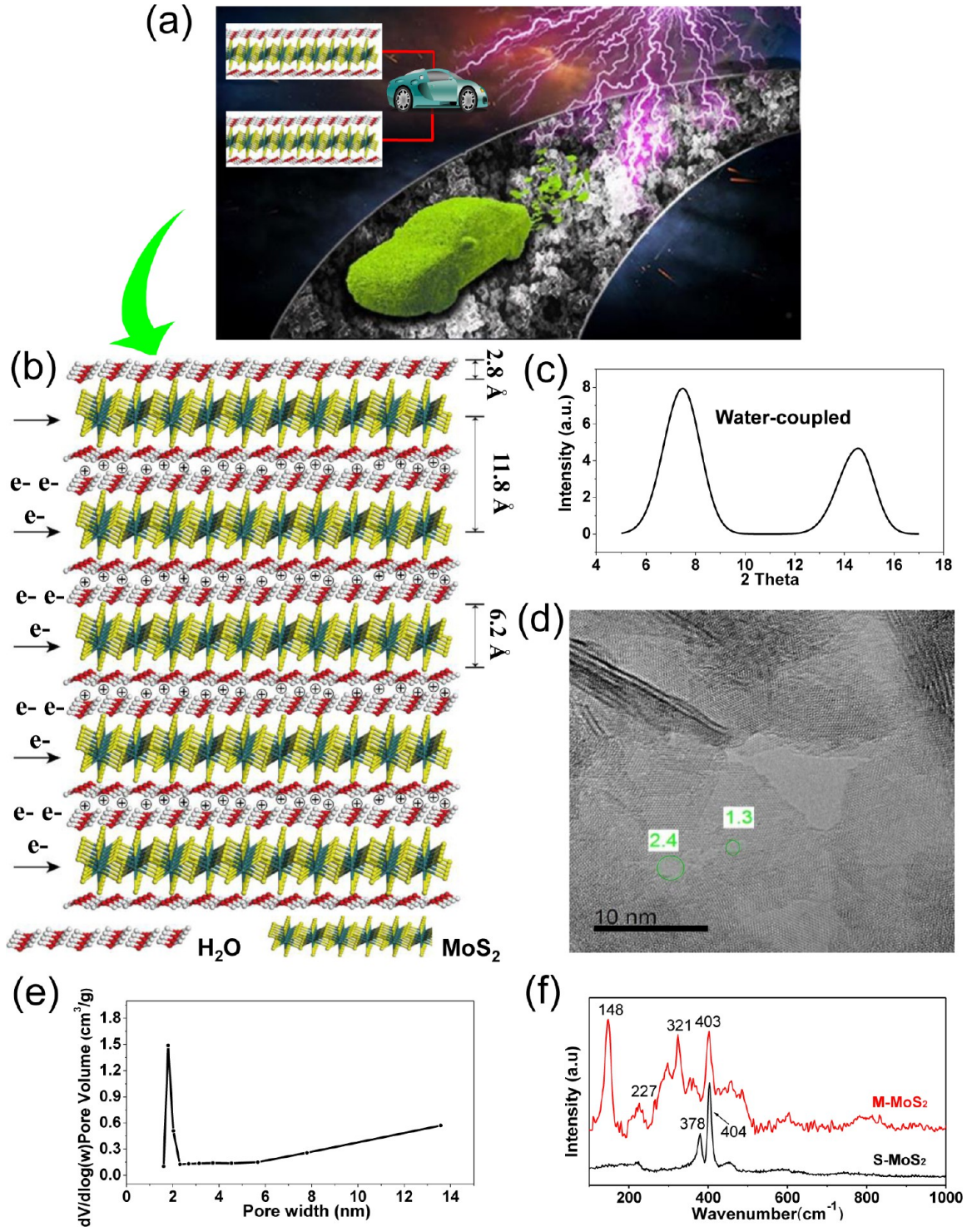

Figure 1. (a) High electrical conductivity of M-MoS_2 builds a "highway" for high speed of electric and hybrid electric vehicles. (b) Schematic illustration of the multilayer M-MoS_2−H_2O based symmetric supercapacitor. (c) XRD of M-MoS_2−H_2O. (d) HRTEM image indicating multilayer and porous structure. (e) Pore-size distribution showing that the average pore size of M-MoS_2 is around 2 nm. (f) Raman spectroscopy of M-MoS_2 and S-MoS_2.

electrochemical storage performance of highly pure metallic phase MoS_2.

Herein, we for the first time demonstrated that the pure and multilayer M-MoS_2 nanosheets deliver a specific capacitance of 380 F/g in Li_2SO_4 electrolyte under the scan rate of 5 mV/s and maintain 105 F/g under the scan rate of 10 V/s. We also examined high rate capacitance performance in H_2SO_4 and Na_2SO_4 electrolytes. As an electrode material for supercapacitor, the resulted multilayer MoS_2 with pure metallic phase has the advantages of more ion-accessible sites and rapid ion/electron transport, giving rise to both faradic and nonfaradic processes occurring during charge−discharge process and thus a high specific capacitance. Moreover, the stability of the M-MoS_2 is associated with the adsorption of a

DOI: 10.1021/acs.nanolett.6b05134
Nano Lett. XXXX, XXX, XXX−XXX

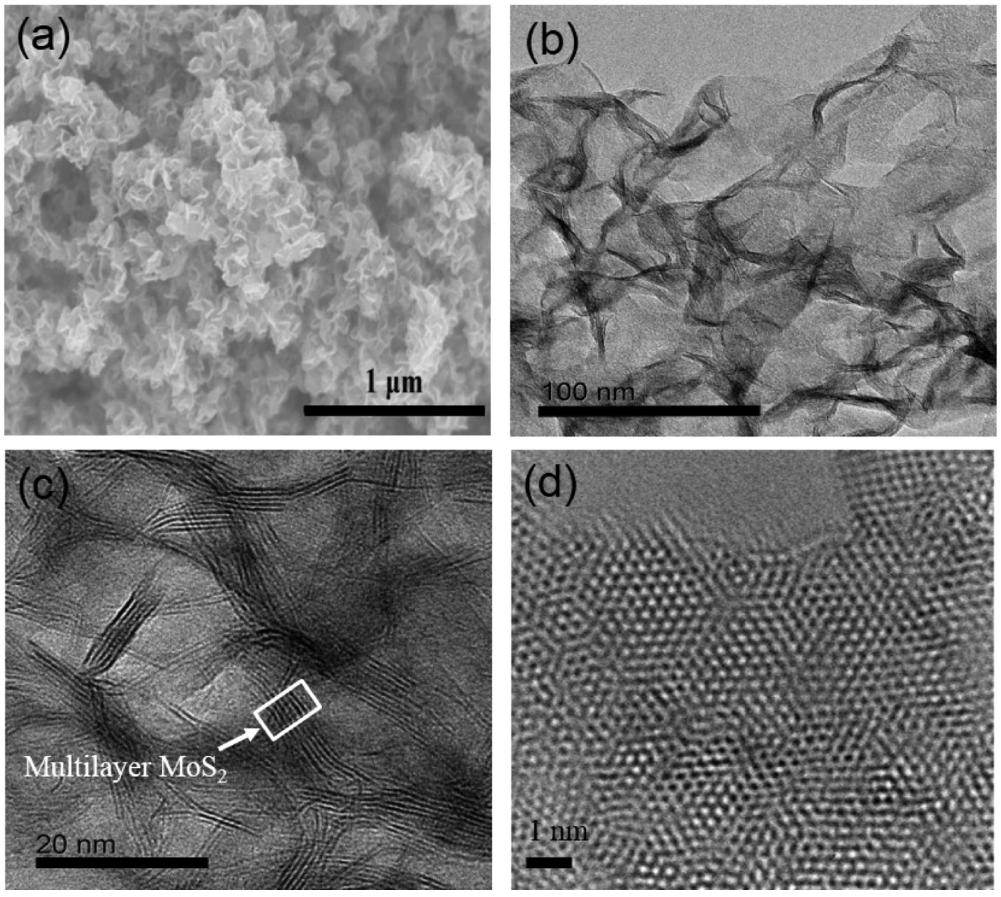

Figure 2. Morphology of as-prepared MoS_2. (a) SEM image of MoS_2 showing a nanosheets structure. (b,c) TEM images with different resolutions indicating multilayer nanostructures. (d) Atomic resolution TEM image of MoS_2 showing atom arrangement.

monolayer of water molecules on both sides of the nanosheets, which reduce restacking and prevent aggregation, resulting in an excellent cycling performance even at a relatively high scan rate.

Results and Discussion. The multilayer and pure metallic phase MoS_2 dispersion is rarely prepared and its intrinsic electrochemical behavior for supercapacitor has never been investigated. The main reason is that metallic phase MoS_2 is unstable under high temperature, pressure, and strain. Here, we employ a hydrothermal method to obtain the multilayer and pure metallic phase MoS_2 as described in Experimental Methods. In our previous work,[14] we found a bilayer of water was attached on the surface of M-MoS_2. The as-prepared M-MoS_2 is highly stable in water due to the reduced stacking of the layered materials, which are separated by water molecules.[14] This ultrafast supercapacitor with multilayer and pure metallic phase MoS_2 as an electrode can potentially be used in a hybrid electrical vehicle to provide high power density, Figure 1a. The mutlilayer M-MoS_2 with bilayer water is able to provide efficient ion and electron transfer pathways due to its unique structure and high electrical conductivity. A schematic of this multilayer superstructure of MoS_2–H_2O system is shown in Figure 1b in which electron transportation is along MoS_2 layer and ion transfer and adsorption is along water molecules. The presence of the water molecule layer along with M-MoS_2 was confirmed with the X-ray powder diffraction (XRD) patterns of wet M-MoS_2 shown in Figure. 1c. The peak at 7.5°, which corresponds to a spacing of 11.8 Å, was assigned to (001)-H_2O for M-MoS_2–H_2O, which contains a bilayer of water molecules between the adjacent layers of MoS_2 nanosheets. The layer thickness of M-MoS_2 ∼ 6.2 Å and the thickness of a monolayer of water 2.8 Å were confirmed in our previous work.[14] The result was also previously confirmed by XRD.[19] This distance between layer and layer can be seen as nanochannels and is suitable for H^+ and Li^+ transportation and adsorption in supercapacitor applications.

Nano-size pores were identified by high-resolution transmission electron microscopy (HRTEM) in the as-prepared MoS_2 nanosheets. Porous structure, an excellent property for supercapacitor, can increase specific surface area and enhance the transportation of ions through two-dimensional planes. Various techniques of making holes were employed in graphene to increase surface area for supercapacitor applications.[1,20] Here, we found nanosize pores in our as-prepared MoS_2 nanosheets. HRTEM displays the size of the pores as around 1–3 nm, Figure 1d. The size of these pores is further confirmed by specific surface area analyzing in Figure 1e, in which 2 nm pores dominate in these MoS_2 nanosheets. These pores contribute to ion accommodation and ion transportation of H^+ and Li^+. This property was never found in previous metallic phase MoS_2 prepared by Li-intercalated semiconductor M-MoS_2. The formed pores in our MoS_2 result from the synthesis condition such as high temperature and high pressure.

To further indicate that the as-synthesized M-MoS_2 is pure metallic phase without semiconductor structure, Raman spectroscopy (Figure 1f) was studied and shows peaks at 148, 227, 321, and 403 cm^{-1} for the feature vibrations of M-MoS_2 sample. The main peak associated with Mo–Mo metallic

DOI: 10.1021/acs.nanolett.6b05134
Nano Lett. XXXX, XXX, XXX–XXX

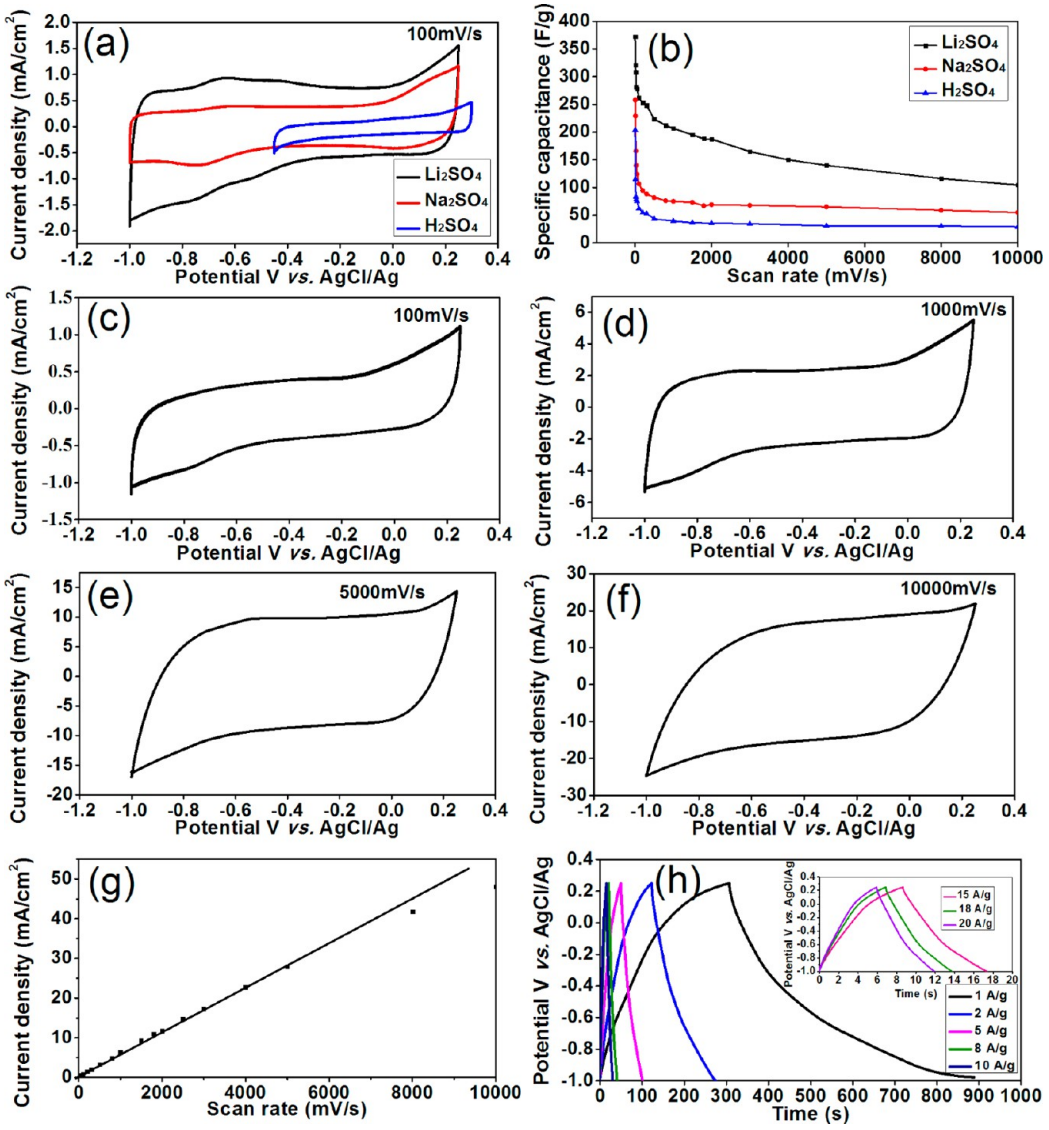

Figure 3. Electrochemical performance of multilayer metallic MoS_2 in standard three electrodes systems. (a) CV curves for three kinds of electrolytes at the same scan rate of 100 mV/s. (b) Galvanostatic charge/discharge performance under different scan rates in three kinds of electrolytes. (c–f) CV curves of M-MoS_2 in 0.5 M Li_2SO_4 electrolyte at different scan rates of 100, 1000, 5000, and 10000 mV/s, respectively. (g) Evolution of specific capacitance versus scan rates. (h) Galvanostatic cycles at different current rates from 1 to 10 A/g in Li_2SO_4 electrolyte.

vibration is located at 148 cm^{-1}, which shows a little higher shift relative to 146 cm^{-1} in our previous experiment. The 150 and 160 cm^{-1} of Raman vibration peaks are usually found in metallic phase MoS_2 obtained by Li-intercalated semiconductor MoS_2.[7,21,22] S-MoS_2 only exhibits typical Raman shifts of 378 and 404 cm^{-1} for E^1_{2g} and A^1_g, respectively.

Two-dimensional multilayer structure of as-prepared M-MoS_2 is confirmed by scanning electron microscopy (SEM) and HRTEM. From SEM, the as-prepared M-MoS_2 sample displays typical nanosheets morphology (Figure 2a). The lateral size is around 100 nm. These nanosheets are connected with each other during the dry process. This close contact network of as-prepared M-MoS_2 with excellent electrical conductivity could facilitate the electron transport. However, these nanosheets did not aggregate like a dense ball that frequently appeared in semiconductor MoS_2, which may lead to inferior electric/ionic transport rate and lower effective contact areas between electrode and electrolyte.[23,24] The better stability of M-MoS_2 ascribe to better hydrophilic property, which is further confirmed by contact angle described in Figure S1. This result suggests that as-prepared M-MoS_2 has a good match of surface energy with water solvent. As a result, it also explains the hydrophilic property of this metallic phase MoS_2. This multilayer structure and hydrophilic property benefit the ion adsorption and transportation for the development of high-rate supercapacitors.

The structures of the as-prepared M-MoS_2 were further characterized by TEM and HRTEM. TEM images show the as-prepared M-MoS_2 is multilayer in Figure 2b and Figure S2. HRTEM images show that the thickness of as-prepared M-MoS_2 layer is about 3.25 nm for ~5 layer nanosheets in Figure 2c and Figure S3. Therefore, the interlayer distance is around 0.65 nm, which is thicker than previous reported result (0.62 nm).[25−29] Our understanding is the multilayer structure of as-prepared M-MoS_2 with double layers H_2O molecular results in increased interlayer distance. This porous hierarchical structure can behave as an "ion-buffering reservoir", which can favor the ion diffusion and assistant the ion adsorption onto the M-MoS_2.

DOI: 10.1021/acs.nanolett.6b05134
Nano Lett. XXXX, XXX, XXX−XXX

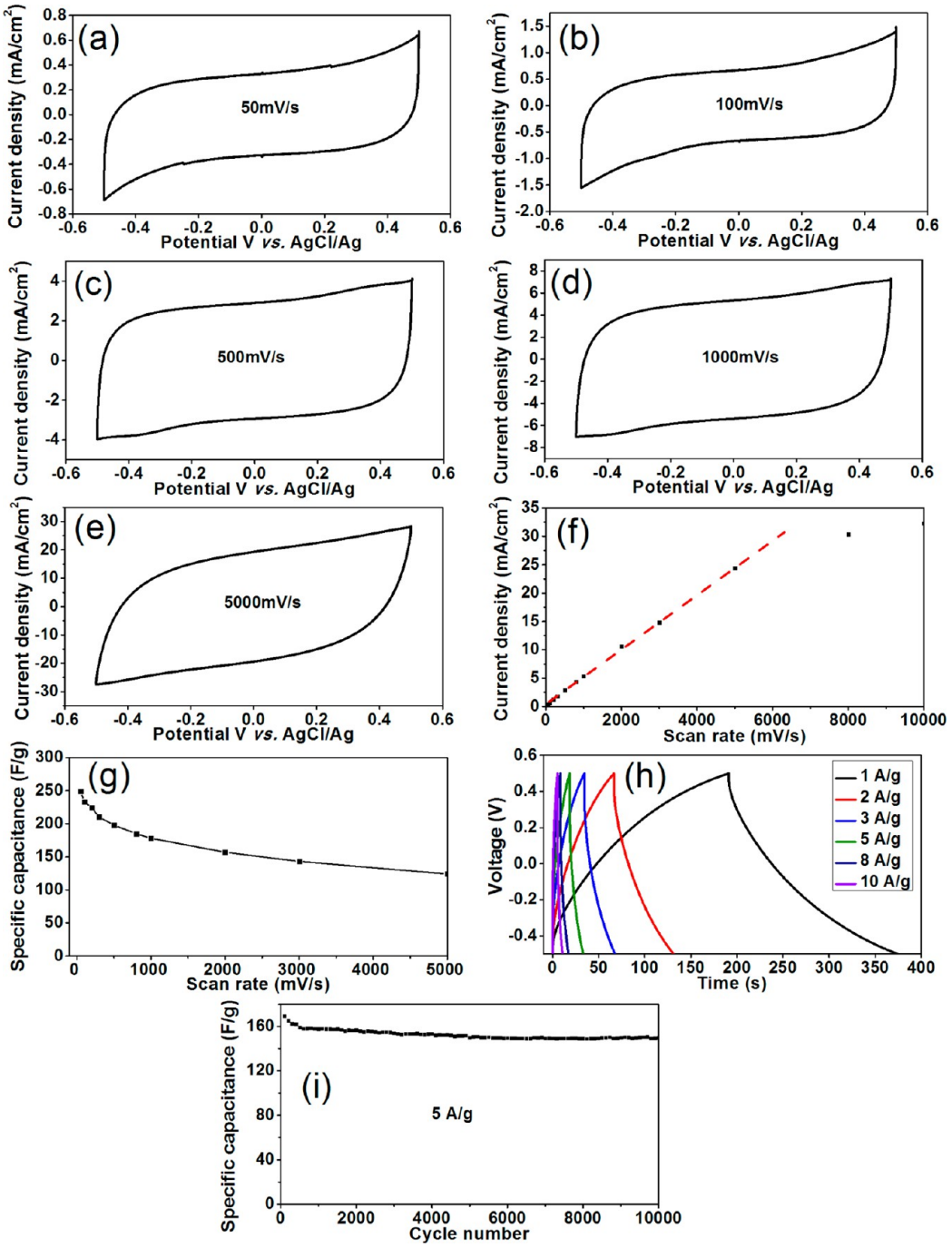

Figure 4. Two electrodes electrochemical characterization of symmetric cells using M-MoS_2 as both electrodes and 1 M Li_2SO_4 as electrolyte. (a–e) CV curves at different scan rates of 50, 100, 500, 1000, and 5000 mV/s, respectively. (f) Evolution of the discharge current density versus scan rates. (g) Evolution of specific capacitance versus scan rates. (h) Galvanostatic charge/discharge profile at different current densities. (i) Long-term cycling performance of the symmetric electrochemical cell devices.

The layer distance varies with the number of layers. In as-prepared M-MoS_2, no amorphous morphology can be detected from HRTEM analysis. We believe that high crystalline MoO_3 as raw materials plays a critical role in forming high quality M-MoS_2. The morphology of this raw material with around 2 μm thickness is displayed in Figure S4. The high crystalline MoO_3 suitable for synthesizing thicker multilayer MoS_2. Atomic resolution TEM (Figure 2d and Figure S5) displays the ordered atom of Mo arrangement of metallic phase MoS_2.

Furthermore, X-ray photoelectron spectroscopy (XPS) provides the information on Mo 3d and S 2p spectra (see Figures S6 and S7). The binding energies located at 228.7 and 231.9 eV correspond to $3d_{5/2}$ and $3d_{3/2}$ orbits of Mo 3d, respectively. The binding energies located at 161.7 and 162.8 eV indicate the S $2p_{3/2}$ and $2p_{1/2}$ orbits, respectively. These binding energy values from Mo 3d and S 2p can only be observed in metallic phase MoS_2 and can never be detected in semiconductor MoS_2. On the basis of XRD, TEM, Raman, and XPS results, we can conclude that the as-prepared MoS_2 is a multilayer MoS_2 with pure metallic phase structure.

The electrochemical storage properties were first investigated in different aqueous solutions, that is, 0.5 M H_2SO_4, Na_2SO_4,

DOI: 10.1021/acs.nanolett.6b05134
Nano Lett. XXXX, XXX, XXX–XXX

and Li_2SO_4. Traditional three electrode configuration was adopted where M-MoS_2 was drop-casted onto glassy carbon as the working electrode and platinum foil and saturated AgCl/Ag as counter and reference electrode, respectively. We reason metallic phase MoS_2 exhibits distinguished capacitive performance compared to previous work because of the multilayers and metallic phase. By discriminating our material from common intercalated 1T formation MoS_2, the symbolic cyclic voltammogram (CV) curves appear to be perfectly overlapped with initial cycle under high scan rates.

The capacitive behaviors in different solutions are compared using CV curves in Figure 3a. Li_2SO_4 and Na_2SO_4 electrolytes could serve a wider electrochemical window between −1 to 0.25 V vs AgCl/Ag, while H_2SO_4 supplies a narrow one between −0.35 and 0.45 V vs AgCl/Ag, which is because MoS_2, especially 1T MoS_2, is a good catalyst for hydrogen evolution reaction in condensed proton environment.[21] The proton is small and can also be transported into nanochannels between MoS_2 layers and pores. Under lower potential, hydrogen would be easily produced, weakening potential application as an anode. Figure 3b further compares specific capacitances for three electrolytes by varying scan rates from 5 mV/s to as high as 10 V/s. Supercapacitor using Li_2SO_4 electrolyte obviously provides a higher capacitive performance than using Na_2SO_4 under the same condition. Apparently Li_2SO_4 plays the best role among all the electrolytes upon capacitive energy storage. The layer space is beneficial for Li^+ intercalation while impedes the bigger Na^+ transportation at the same time. At the scan rates from 100 to 5000 mV/s, the obtained CV curves are close to the rectangular shape (Figure 3c−e), indicating the fast charge propagation within the electrodes. By increasing the scan rate up to 10 V/s and above, a certain deviation from the rectangular shape is observed for the CV curves (Figure 3f). The scan rate versus current density performs a straight linear relationship (Figure 3g). Both the rectangular shape and linear coefficient indicate good capacitive behavior. Specifically, MoS_2 electrode delivers a maximum specific capacitance of 380 and 170 F/g under the scan rates of 5 and 10000 mV/s, respectively. Galvonastatic charge/discharge (GCD) measurements are performed in Li_2SO_4 aqueous electrolyte at current rates of 1, 2, 5, 8, and 10 A/g (Figure 3h). All curves possess a near symmetric triangular shape, especially under high current density, indicating the excellent performance of the M-MoS_2 electrode. The specific capacitance values derived from the GCD curves at 1 A/g is in well agreement with those from CV curves. In addition, the discharge capacity in Figure 3h is slightly larger than the charge capacity at the current rates of 1 and 2 A/g, indicating hydrogen evolution reaction occurs at a very negative potential (−0.8 V versus AgCl/Ag) of the working electrode. This is because MoS_2, especially M-MoS_2, is a favorable catalyst for hydrogen evolution reaction.

To evaluate the energy and power density of this bulk metallic MoS_2 in supercapacitor, symmetric MoS_2 supercapacitor cells were prepared and assembled in aqueous Li_2SO_4 electrolyte. CV curves with similar and more uniform rectangular shape were obtained at different scan rates from 10 to 5000 mV/s (Figure 4a−e). When further increasing the scan rate up to 10 000 mV/s, exterior rectangular deformation of the CV curve would happen. Figure 4f shows the linear trend of current density function as scan rates; we confirm that 5000 mV/s was the fast charge−discharge rate employed for the device. What counts is that the trend for high rate scanning was designated for MoS_2 itself as there is no other additive or binder during electrode preparation but pure MoS_2. To proceed further, we notice that the rate capability is in agreement with the material itself with 50% capacity retention by increasing from 50 to 5000 mV/s (Figure 4g). Moreover, the specific capacitance under 50 mV/s is 249 F/g, which accounts for 89.9% of three electrode system (278 F/g at 50 mV/s). To date, the bulk MoS_2 electrode displays the highest capacitance over such a large range of scan rates. GCD curves of the M-MoS_2 electrode are recorded with various current densities to further evaluate the electrochemical performance. As shown in Figure 4h, these typical triangular-shape charge/discharge curves exhibit good symmetry and fairly linear slopes at different current densities, again demonstrating the ideal capacitive characteristic. The cycling performance of this symmetric supercapacitor was measured over 10 000 charging/discharging cycles at 5 A/g (Figure 4i). The specific capacitance is maintained at 150 F/g and the capacity retention is up to 88% even after 10 000 cycles. This high current density and high capacity retention of the M-MoS_2 symmetry capacitor pave the way for the promising applications in electrical vehicle, wearable electronics, and so forth. Furthermore, we tested the control samples of S-MoS_2 and mixture MoS_2. Figure S8a shows CV curves of M-MoS_2, S-MoS_2, and mixture-MoS_2 (S-MoS_2/M-MoS_2 = 1:1 by weight) at a scan rate of 100 mV/s. Clearly, M-MoS_2 reflects the largest area of the curve among the three samples, which indicates its superior capacitive performance. Derived from GCD curves in Figure S8b, M-MoS_2, S-MoS_2, and mixture-MoS_2, respectively show a discharge capacitances of 183, 7, and 61 F/g at a 1A/g. The obtained Nyquist plots are shown in Figure S8c. Typically, the intersecting point with the real axis at high frequency indicates the equivalent series resistance (Rs) and the high-frequency semicircle corresponds to the charge transfer resistance (Rct). The relatively low Rs and Rct values of M-MoS_2 roughly estimated from Nyquist plots implies that the M-MoS_2 has smaller internal resistance and faster electrochemical kinetics compared with S-MoS_2 and Mixture-MoS_2. We further evaluate the energy and power density of this bulk M-MoS_2, they are 51 Wh/kg and 1000 W/kg under 1 A/g. This result is displayed in Figure S9

The excellent electrochemical performances of the M-MoS_2 are ascribed to their hydrophilicity and high electrical conductivity, as well as multilayers structures with abundant nanochannels. The M-MoS_2−H_2O functions in various aspects, such as (1) the high electrical conductivity of metallic phase MoS_2 greatly enhances the electric conductivity of the electrode and benefits the charge transfer; (2) its inner porous structure and superhydrophilic property provide an efficient condition for diffusion of electrolyte ion; (3) the adsorption of a monolayer of water molecules on both sides of the nanosheets reduce restacking and remarkably accommodates the volume variations resulting in satisfying cycling stability even at relatively high scan rates; and (4) no other additive or binder during electrode preparation but pure M-MoS_2 allows efficient utilization of active material and greatly improves the electrical conductivity and Li^+ diffusion performance.

Conclusions. In conclusion, multilayer highly pure and water-coupled M-MoS_2 nanosheets were synthesized and first applied to the supercapacitor. The obtained M-MoS_2 nanosheets show excellent electrochemical performance for supercapacitor in aqueous electrolyte. Good electrical conductivity of M-MoS_2 enables high electron transfer efficiency and benefits energy storage for supercapacitor. Meanwhile, the monolayer

DOI: 10.1021/acs.nanolett.6b05134
Nano Lett. XXXX, XXX, XXX−XXX

water molecules in the nanochannels assist the ion transfer and adsorption. This M-MoS_2 has outstanding adhesion onto substrates and is employed as a binder-free and carbon-free electrode. We found the best electrolyte is Li_2SO_4 because the layer distance of this MoS_2 is around 1.18 nm, which is suitable for the high rate adsorption/desorption of ion onto/from MoS_2 layers. The M-MoS_2−H_2O electrode delivers high capacitance and excellent rate performance not only in three electrodes systems but also in symmetrical two electrode capacitors. High energy density and power density are obtained that are 51 and 1000 W/kg under 1 A/g current density, respectively. To summarize, we for the first time realized this special multilayer and water-coupled M-MoS_2 for high rate supercapacitor with extraordinary performance. Meanwhile, water-coupled M-MoS_2 sample can be dispersed uniformly in water. Therefore, the highly conductive water-coupled M-MoS_2 is promising for the application as high rate supercapacitor.

Experimental Methods. *M-MoS_2 and S-MoS_2 Preparation.* Twelve milligrams of MoO_3 (Fisher Scientific, U.S.A.), 14 mg of thioacetamide (Sigma-Aldrich, U.S.A.), and 100 mg of urea (Fisher Scientific, U.S.A.) were added into 10 mL of deionized (DI) water, followed with 1 h of magnetic stirring at 500 rpm. Then the well-mixed solution was transferred to an autoclave (Parr Instrument Corp.) and kept in a furnace for 18 h at 200 °C for M-MoS_2 and 240 °C for S-MoS_2. Then the autoclave was cooled down in room temperature. The as-prepared metallic MoS_2 was washed with DI water and ethanol individually and then stabilized in the mixture of DI water and ethanol.

Sample Characterization. Transmission Electron Microscopy Observations. TEM and HRTEM imaging and electron diffraction were performed on a FEI Tecnai G2 F20 S-Twin microscope operated at an accelerating voltage of up to 100 kV. The TEM sample was prepared by ultrasonic at 500 W for ∼5 min, and 25 μL of supernatant was dropped onto holey carbon grids.

Scanning Electron Microscopy Observations. Morphology and composition of the as-prepared MoS_2 was characterized by an ultrahigh resolution scanning electron microscopy (Hitachi S4800), which has an optimum resolution of 1.4 nm. The MoS_2 film was imaged under ultrahigh resolution mode at 3 kV accelerating voltage to reveal the morphology. For composition analysis, uncoated samples were analyzed by the accessorily equipped energy dispersive X-ray spectroscopy at 15 kV accelerating voltage.

X-ray Photoelectron Spectroscopy. XPS was conducted using an Axis Ultra DLD (Kratos) system. The vacuum of the chamber was 1×10^{-9} Torr. A monochromatic aluminum K source with a source power of 150 W (15 kV × 10 mA) was used. The pass energy was 160 eV for wide scans and 40 eV for narrow scans.

Raman Spectroscopy. Raman spectroscopy was performed using a LabRam HR800 UV NIR and 532 nm laser excitation with working distances on a 50× lens. The Raman spectra of the metallic MoS_2 were recorded by depositing the samples on silicon substrates.

XRD Patterns. XRD patterns of MoS_2 were recorded for two θ-values ranging from 4° to 18° to characterize the interlayer spacing. The characterization was performed on a Bruker AXS-D8 Advance powder X-ray diffractometer using Cu/Ka radiation (λ = 1.5406 Å) with a step size of 0.02° and a dwell time of 3.0 s.

Surface Area Analyzer. Surface area was measured on Quantachrome NOVA 2200e.

Contact Angle Measurements. The contact was measured by drop casting a droplet of water (5 μL) on the sample film and measuring the angle between the droplet and MoS_2. The contact angle was determined by contact angle tester (DataPhysics instruments GmbH, Filderstadt, Germany).

Electrochemical Analysis. Electrochemical measurements were conducted on Biologic SP150. For tests in three-electrode cell configuration, 0.5 M H_2SO_4, Li_2SO_4, and Na_2SO_4 were used as the electrolyte solutions, and saturated AgCl/Ag and platinum foil were used as reference and counter electrode, respectively. Cyclic data was collected between −0.25−0.55 V versus AgCl/Ag with scan rates ranging from 10 to 300 000 mV/s. The voltage window was chosen to avoid hydrogen evolution and oxidation beyond the scope. Typically, prior to drop-casting MoS_2 onto the surface of glassy carbon working electrode, MoS_2 was sonicated for at least 20 min. Ten micrograms of active material was casted on glassy carbon and dried in air. The active material mass loading was about 0.14 mg/cm^2. The specific capacitance (C, F/g) is calculated according to equation $C = It/V$, where I is the mass normalized current (A/g), t is the discharge time (s), and V is the potential range (V). Energy density (E, Wh/kg) and power density (W/kg) of the materials are calculated based on the total mass of electrodes by the following equations: $E = 0.5CV^2$ and $P = E/T$, respectively. T is the discharge time of the charge−discharge curves from where the specific capacitance is calculated.[13]

■ ASSOCIATED CONTENT

Supporting Information

The Supporting Information is available free of charge on the ACS Publications website at DOI: 10.1021/acs.nanolett.6b05134.

Contact angle, TEM, SEM, HRTEM, Raman, XPS, power and energy density (PDF)

■ AUTHOR INFORMATION

Corresponding Author

*E-mail: h.zhu@neu.edu.

ORCID

Hongli Zhu: 0000-0003-1733-4333

Author Contributions

X. G., Y. Z., and Y. H. contributed equally.

Notes

The authors declare no competing financial interest.

■ ACKNOWLEDGMENTS

H.Z. acknowledges the financial startup support and Tier 1 award from Northeastern University. We also thank Center for Nanoscale System (CNS) in Harvard University for using their facilities.

■ REFERENCES

(1) Zhu, Y.; Murali, S.; Stoller, M. D.; Ganesh, K.; Cai, W.; Ferreira, P. J.; Pirkle, A.; Wallace, R. M.; Cychosz, K. A.; Thommes, M. *Science* **2011**, *332*, 1537−1541.

(2) Lin, T.; Chen, I.-W.; Liu, F.; Yang, C.; Bi, H.; Xu, F.; Huang, F. *Science* **2015**, *350*, 1508−1513.

(3) Ji, H.; Zhao, X.; Qiao, Z.; Jung, J.; Zhu, Y.; Lu, Y.; Zhang, L. L.; MacDonald, A. H.; Ruoff, R. S. *Nat. Commun.* **2014**, *5*, 3317.

DOI: 10.1021/acs.nanolett.6b05134
Nano Lett. XXXX, XXX, XXX−XXX

(4) Yang, X.; Cheng, C.; Wang, Y.; Qiu, L.; Li, D. *Science* **2013**, *341*, 534−537.
(5) Faraji, S.; Ani, F. N. *Renewable Sustainable Energy Rev.* **2015**, *42*, 823−834.
(6) Mak, K. F.; Lee, C.; Hone, J.; Shan, J.; Heinz, T. F. *Phys. Rev. Lett.* **2010**, *105*, 136805.
(7) Lukowski, M. A.; Daniel, A. S.; Meng, F.; Forticaux, A.; Li, L.; Jin, S. *J. Am. Chem. Soc.* **2013**, *135*, 10274−10277.
(8) Lee, K.; Kim, H. Y.; Lotya, M.; Coleman, J. N.; Kim, G. T.; Duesberg, G. S. *Adv. Mater.* **2011**, *23*, 4178−4182.
(9) Yang, M.; Jeong, J.-M.; Huh, Y. S.; Choi, B. G. *Compos. Sci. Technol.* **2015**, *121*, 123−128.
(10) Bissett, M. A.; Kinloch, I. A.; Dryfe, R. A. *ACS Appl. Mater. Interfaces* **2015**, *7*, 17388−17398.
(11) Wang, J.; Wu, Z.; Hu, K.; Chen, X.; Yin, H. *J. Alloys Compd.* **2015**, *619*, 38−43.
(12) Savjani, N.; Lewis, E. A.; Bissett, M. A.; Brent, J. R.; Dryfe, R. A.; Haigh, S. J.; O'Brien, P. *Chem. Mater.* **2016**, *28*, 657.
(13) Acerce, M.; Voiry, D.; Chhowalla, M. *Nat. Nanotechnol.* **2015**, *10*, 313−8.
(14) Geng, X.; Sun, W.; Wu, W.; Chen, B.; Al-Hilo, A.; Benamara, M.; Zhu, H.; Watanabe, F.; Cui, J.; Chen, T. P. *Nat. Commun.* **2016**, *7*, 10672.
(15) Py, M.; Haering, R. *Can. J. Phys.* **1983**, *61*, 76−84.
(16) Mattheiss, L. *Phys.Rev. B* **1973**, *8* (8), 3719.
(17) Zheng, J.; Zhang, H.; Dong, S.; Liu, Y.; Nai, C. T.; Shin, H. S.; Jeong, H. Y.; Liu, B.; Loh, K. P. *Nat. Commun.* **2014**, *5*, 2995.
(18) Eda, G.; Fujita, T.; Yamaguchi, H.; Voiry, D.; Chen, M.; Chhowalla, M. *ACS Nano* **2012**, *6*, 7311−7317.
(19) Qin, X. *Scanning tunneling microscopy of layered materials*; Ph.D. Theses, Simon Fraser University, Burnaby, British Columbia, 1992.
(20) Ervin, M. H. *Nanotechnology* **2015**, *26*, 234003.
(21) Voiry, D.; Salehi, M.; Silva, R.; Fujita, T.; Chen, M.; Asefa, T.; Shenoy, V. B.; Eda, G.; Chhowalla, M. *Nano Lett.* **2013**, *13*, 6222−6227.
(22) Bai, S.; Wang, L.; Chen, X.; Du, J.; Xiong, Y. *Nano Res.* **2015**, *8*, 175−183.
(23) Li, Y.; Wang, H.; Xie, L.; Liang, Y.; Hong, G.; Dai, H. *J. Am. Chem. Soc.* **2011**, *133*, 7296−7299.
(24) Yu, H.; Ma, C.; Ge, B.; Chen, Y.; Xu, Z.; Zhu, C.; Li, C.; Ouyang, Q.; Gao, P.; Li, J. *Chem. - Eur. J.* **2013**, *19*, 5818−5823.
(25) Tributsch, H.; Bennett, J. *J. Electroanal. Chem. Interfacial Electrochem.* **1977**, *81*, 97−111.
(26) Kong, D.; Wang, H.; Cha, J. J.; Pasta, M.; Koski, K. J.; Yao, J.; Cui, Y. *Nano Lett.* **2013**, *13*, 1341−1347.
(27) Zheng, X.; Xu, J.; Yan, K.; Wang, H.; Wang, Z.; Yang, S. *Chem. Mater.* **2014**, *26*, 2344−2353.
(28) Ma, C.-B.; Qi, X.; Chen, B.; Bao, S.; Yin, Z.; Wu, X.-J.; Luo, Z.; Wei, J.; Zhang, H.-L.; Zhang, H. *Nanoscale* **2014**, *6*, 5624−5629.
(29) Zhang, Z.; Li, W.; Yuen, M. F.; Ng, T.-W.; Tang, Y.; Lee, C.-S.; Chen, X.; Zhang, W. *Nano Energy* **2015**, *18*, 196−204.

■ NOTE ADDED AFTER ASAP PUBLICATION

This paper was published on the Web on February 2, 2017, with a minor error in the Title, along with a few minor text corrections throughout the paper. The corrected version was reposted on February 3, 2017.

DOI: 10.1021/acs.nanolett.6b05134
Nano Lett. XXXX, XXX, XXX−XXX